A High-Throughput Platform for Rapid Adaptation of DNA Aptamers to SARS-CoV-2 Evolution

Yujie He[1†], Zhenglin Yang[2†], Yu-An Kuo[1], Yuting Wu[2], Diego Fonseca-Albert[1], Kyle K. Le[1], Jeffrey Guo[1], Yanxing Wang[1], Anh-Thu Nguyen[1], Yuan-I Chen[1], Sohyun Kim[1], Wei-Ru Chen[1], Saeed Seifi[1], Soonwoo Hong[1], Trung Duc Nguyen[1], Yinong Chen[3], Pengyu Ren[1], Yi Lu[2] and Hsin-Chih Yeh[1,4,]*

[1]Department of Biomedical Engineering, University of Texas at Austin, Austin, TX, USA
[2]Department of Chemistry, University of Texas at Austin, Austin, TX, USA
[3]Department of Biomedical Engineering, Johns Hopkins University, Baltimore, MD, USA
[4]Texas Materials Institute, University of Texas at Austin, Austin, TX, USA
†These authors contributed equally
*Corresponding author: tim.yeh@austin.utexas.edu

ABSTRACT

Rapid pathogen evolution threatens public health by eroding the effectiveness of vaccines, therapeutics, and diagnostic tools. Although spike protein targeting monoclonal antibodies (mAbs) were developed within 10-12 months of the initial outbreak to serve as key theranostic agents, their redesign has struggled to keep pace with viral evolution, rendering many neutralizing antibodies ineffective. Here we demonstrate a novel platform that combines a random-rational hybrid library diversification with high-throughput *MiSeq* screening to rapidly reprogram aptamers against emerging SARS-CoV-2 spike variants. Interactions between 3 different spike proteins and 11,806 unique aptamer variant designs were profiled within a few days. Starting from a 40-nt aptamer originally selected against wild-type (WT) spike protein, our screen identified a Delta-binding mutant with a 4-fold affinity improvement and an Omicron-binding mutant that converted undetectable binding into nanomolar affinity. We also identified a WT-selective mutant with substantially reduced affinity for Delta, as well as previously unrecognized bases that critically contribute to spike recognition. Integrating high-throughput binding data with molecular dynamics simulations further revealed sequence-dependent structural features underlying variant-specific aptamer-spike interactions. Finally, we developed a sensor based on the identified WT-selective aptamer mutant, enabling highly specific detection of the WT spike protein with robust performance. Together, this work establishes a rapid and adaptable aptamer engineering platform for rapid adaptation of aptamers to evolving pathogens in future pandemics.

INTRODUCTION

By December 2025, the cumulative number of confirmed COVID-19 cases and deaths worldwide had reached 779 million and 7.1 million, respectively[1]. A major challenge in halting this pandemic arises from the rapid evolution of SARS-CoV-2 virus. Since the outbreak in 2019, the World Health Organization (WHO) has identified five variants of concerns (VOCs), including Alpha, Beta, Gamma, Delta and Omicron[2–6], These variants exhibit markedly higher transmissibility than the original strain[7,8], leading to extended quarantine, increased hospitalization and vaccine breakthrough infections[9–15]. To combat the COVID-19 pandemic, at least 17 monoclonal antibodies (mAbs) for both patient treatment and SARS-CoV-2 detection were successfully developed and granted Emergency Use Authorization (EUA) by the U.S. FDA in late 2020[16,17]. However, these authorizations were later revoked[18,19] as continuous viral evolution rendered these antibodies ineffective[20,21]. Developing new mAbs at pandemic speed and subsequently optimizing them to

keep pace with viral mutations[18,20] remain a formidable challenge. Therefore, a modular, highly adaptable platform that can be rapidly reprogrammed and deployed for both the diagnosis and therapeutic applications of emerging viral variants is urgently needed to support rapid responses for future pandemics[22].

Highly adaptable functional nucleic acid technologies can fulfill this need. Analogous to mAbs, DNA aptamers identified through SELEX (Systematic Evolution of Ligands by EXponential enrichment) process[23–25] can bind spike proteins with high affinities (k_d values down to the sub nM range[26–28]). For instance, a 40-nt DNA aptamer Apt2 developed by Zu and co-workers[27] exhibits a k_d of 2 nM when binding spike protein derived from the original wild-type (WT) strain and costs only ~$0.72 per nanomole to synthesize commercially. In the past few years, dozens of DNA aptamers have been developed to bind different epitopes of the SARS-CoV-2 virus, such as various domains, especially the receptor-binding domain (RBD), of the spike protein[26,28–31] and nucleocapsid proteins[32]. Although some can bind multiple viral strains[33–35], most of them faced limited cross-variant robustness. For instance, we found that Apt2 exhibits negligible binding to the spike protein of one of the Omicron subvariants, $\text{Omicron}_{\text{XBB}}$ (**Fig. 1C**), possibly because Apt2 was originally selected against the WT strain, whereas the subvariant harbors 39 amino-acid mutations in its spike protein (21 of them are within the RBD). Although aptamers, compared to mAbs, are inherently more amenable to rapid reengineering to accommodate viral mutations, the conventional de novo approach to develop DNA aptamers (i.e., SELEX[23]) relies on time-consuming iterative enrichment and counterselection steps to isolate strong and highly specific binders from a highly diverse library (~10^{15} sequences), limiting its ability to generate new aptamers quickly enough to keep pace with viral evolution during a pandemic.

To overcome this limitation, we developed a pipeline based on a repurposed Illumina next-generation sequencing (NGS) platform[36–50] that enables massively parallel, quantitative evaluation of aptamer–protein interactions across 10^4-10^7 (depending on the flow cell type) closely related sequences within a single run[51–55]. Repurposed NGS flow cells have provided a powerful platform to directly study interactions between target analytes and libraries of DNA[40,53], RNA[45,46], modified bases[56], and peptide[42,47]. Previously, we employed a repurposed NGS method known as CHAMP[53] (Chip-Hybridized Association-Mapping Platform, which eliminates the need to modify Illumina's sequencing protocol) to screen fluorescent nanomaterial[57], optimize and diversify the photophysical properties of fluorogenic DNA[55] and RNA[58] aptamers, while related studies[56,59–61] have demonstrated the broader utility of NGS-based platforms for aptamer characterization and optimization. While previous work established a high-throughput screening framework for nanomaterial characterization, its ability to rapidly adapt to the emerging viral variants remains limited.

To address this, we developed a random-rational hybrid library design (**Fig. 1D**) integrated with CHAMP-based screening. This approach is based on the premise that, for certain virus-binding aptamers, adaptation to new variants does not require complete redesign, but can be achieved through targeted diversification around a functional seeding sequence. By preserving controlled diversity in this local sequence space, the platform enables rapid and directed aptamer reengineering without the need for de novo selection. Using this strategy, we screened 11,806 variants directly on a repurposed NGS flow cell. Apt2 served as an ideal model due to its well-characterized WT RBD binding and early development during the pandemic. By simultaneously measuring binding affinities across all variants without enrichment or loss of sequence diversity, this platform enables systematic exploration of sequence-function relationships and accelerates adaptation to new SARS-CoV-2 variants from months to days. The reusability of the flow cell further supports iterative testing against multiple viral variants on the same platform, facilitating rapid identification

of both affinity-enhanced and strain-selective binders. To the best of our knowledge, this study is the "first to demonstrate repurposed NGS screening as a rapid adaptation strategy for reengineering aptamer recognition against evolving pathogen variants.

In this study, we show that this high-throughput screening strategy enables rapid reengineering of aptamers to adapt to emerging SARS-CoV-2 variants from a single WT binder. Specifically, targeted diversification yielded variants with enhanced binding to Delta, restored affinity toward $\text{Omicron}_{\text{XBB}}$ from undetectable levels to the nM range and enabled the generation of WT-selective binders with minimal cross-reactivity. The high-throughput profiling also revealed that beyond the loop motif, the upper stem region plays a critical role in spike protein recognition. Further molecular dynamics (MD) simulations offered structural rationales for the improved binding characteristics of the optimized aptamer mutants. Finally, a WT-selective aptamer was translated into a strand-displacement fluorescent sensor, achieving highly specific detection with robust performance in complex biological matrices. Together, these results demonstrate a scalable strategy for rapidly adapting molecular recognition elements to evolving pathogens, providing a practical framework for next-generation theranostic development.

RESULTS

Designing an Apt2 Variant Pool for Aptamer Diversification

We selected Apt2, a 40-nt DNA aptamer developed by the Zu group[27] against the SARS-CoV-2 WT spike protein (hereafter referred to as WT in short), as the seeding aptamer to explore neighboring sequence variants capable of binding the Delta (B.1.617.2) and $\text{Omicron}_{\text{XBB}}$ spike proteins. Apt2 was chosen because of its well-characterized WT RBD binding and its early development during the pandemic. Delta and $\text{Omicron}_{\text{XBB}}$ were selected as model viral variants because both raised major global concern and complicated pandemic control through increased transmissibility and reduced immune effectiveness[5,13–15,20]. They also represent distinct stages and magnitudes of SARS-CoV-2 evolution, with Delta and $\text{Omicron}_{\text{XBB}}$ carrying 9 and 39 spike amino-acid mutations, respectively, and emerging approximately 1 and 3 years after the original strain (**Fig. 1A**). Together, these features make Apt2 and these two variants suitable models for evaluating whether local sequence diversification can rapidly adapt an existing aptamer to evolving viral targets.

The Apt2 folds into a hairpin structure, as predicted by mFold[62], with the 20-nt loop corresponding to the binding motif identified through the SELEX process (**Fig. 1B**). We first tested the binding affinity of the original Apt2 against the aforementioned three spike proteins using an enzyme-linked oligonucleotide assay[63] (ELONA**, fig. S1A**). The results (**Fig. 1C**) were consistent with the structural and sequence divergence of these spike proteins, showing that Apt2 binds strongly to the WT (k_d ~2±0.4 nM), moderately to the Delta spike protein (k_d ~89±10 nM) and becomes undetectable with the $\text{Omicron}_{\text{XBB}}$ spike protein (no stable k_d determined). No binding affinity to any of the three spike proteins was observed from the scramble sequence (Scr). A mutant pool was designed using a random-rational hybrid algorithm to ensure a controlled diversity in this local sequence space, which included four subgroups: single mutations (120 sequences, 1.08%), double mutations (6,508 sequences, 58.7%), indels (single insertions or deletions, 152 sequences, 1.37%), and doped (i.e., partially randomized[64,65]) mutants (4,500 sequences, 37.6%, generated with a mutation rate of 10% within the 20-nt loop motif and filtered to remove duplicates with the other subgroups) (**Fig. 1D**). Based on the calculation (**Methods** and **fig. S2**), most doped mutants contain either triple (59%) or quadruple (28%) mutations, representing a well-controlled degree of

diversity for optimizing aptamers for emerging variants.

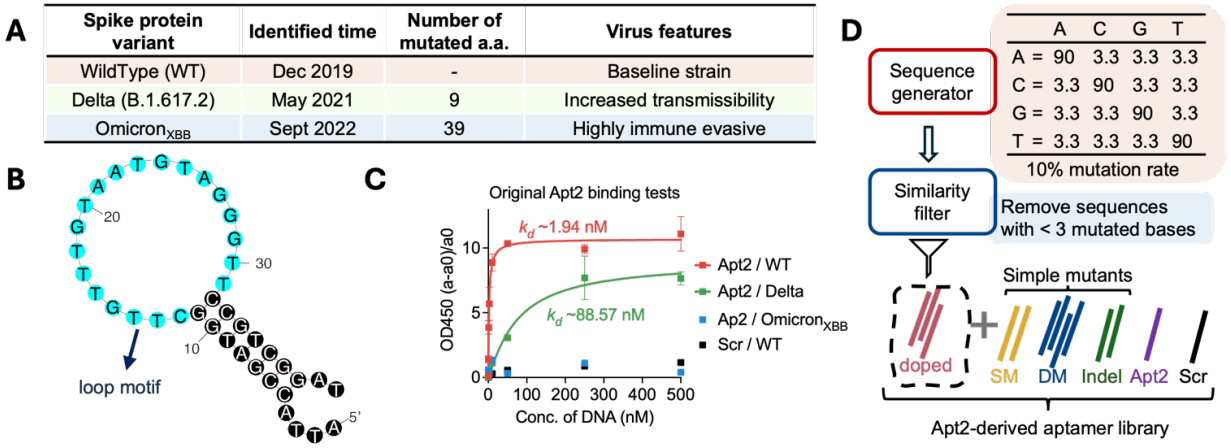

Fig. 1. Apt2 chosen as the seeding strand for SARS-CoV-2 spike protein aptamer diversification and screening. (**A**) The selected SARS-CoV-2 spike protein (trimer) variants in the experiment. Both Delta and Omicron$_{XBB}$ drove major global waves during the COVID-19 pandemic through their mutations, with the more recent one Omicron$_{XBB}$ being distinctly different than the original strain. a.a.: amino acid(s). (**B**) The secondary structure of Apt2 as predicted by mFold, with the 20-nt loop motif region identified by the previous SELEX, highlighted in light blue. (**C**) Characterization of the seeding aptamers and the negative control sequence with ELONA. k_d(Apt2/WT) ~2±0.4 nM; k_d(Apt2/Delta) ~89±10 nM. (**D**) Aptamer library design for chip screening. SM: single mutants; Indel: insertion and deletion mutants; DM: double mutants; Scr: the scrambled sequence.

High-throughput Screening of Apt2-derived Pool on an Illumina NGS Flow Cell

To screen the pool in a high-throughput manner, we synthesized the library, added sequencing adapters and loaded it onto an Illumina *MiSeq* flow cell (**Fig. 2A**). Before screening, we first confirmed that the sequencing adapters and primers did not disrupt aptamer binding (**figs. S3-S4**). After sequencing, the strands were denatured, and the flow cell was thoroughly rinsed to remove any excess dyes. The fiducial marker PhiX was then labeled with an Atto488-tagged PhiX probe and imaged (**Fig. 2B**) for mapping purpose[51,55]. The His-tagged spike protein was injected to the flow cell, captured by the displayed binders, and secondarily labeled via an Alexa647-conjugated anti-His-tag antibody. The fiducial markers and bound proteins were imaged under fluorescence microscopy using two different filter cubes). The spike protein binding capacity of each sequence was estimated by the mean fluorescence intensity among its duplicates on the chip (**Methods**). By digesting the proteins and denaturing the DNAs, the same flow cell could be reset to its initial state for sequential screening of binders against another protein target (**Fig. 2C**). This approach allows the binding characterization of the entire pool against multiple SARS-CoV-2 spike protein variants on a single chip, thereby reducing experimental cost and material usage.

As a proof-of-concept, we performed the first screen against WT. Fiducial markers' patterns were captured under the FITC channel, and those of captured spike proteins were collected under the Cy5 channel (**Fig. 2D, upper**). The positions of the bright FITC puncta matched the coordinates recorded in the FASTQ file (**Fig. 2D, left**), confirming successful image alignment. Within the field of view (FOV), positions corresponding to Apt2 co-localized with several bright Alexa647 puncta, whereas those corresponding to Scr remained dark (**Fig. 2D, right**). These results demonstrated that binding was visualized as planned. Next, we regenerated the flow cell and

performed another round of screening against Omicron$_{XBB}$. We compared the acquired fluorescence intensities with the original Apt2 and Scr signals. The results showed that Apt2 exhibited significantly higher fluorescence intensity than Scr when introducing WT (**Fig. 2E, left**), while the brightness of them was similar when the protein target switched to the Omicron$_{XBB}$ (**Fig. 2E, middle**), which agreed with our ELONA results that Apt2 is a strong binder to the WT while a non-binder to the Omicron$_{XBB}$ (**Fig. 1C**). A third round of screening against Delta was then performed following the chip regeneration (**Fig. 2E, right**).

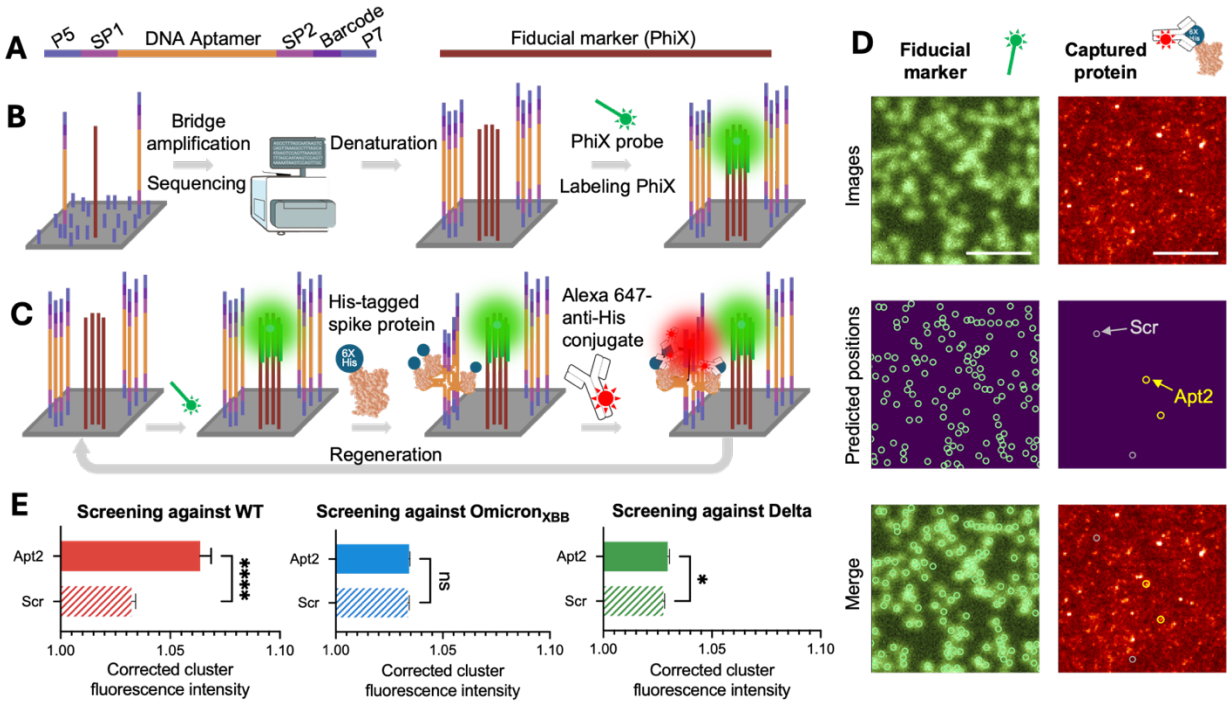

Fig. 2. Overview of SARS-CoV-2 spike protein variants specific aptamer identification on Illumina NGS chips. (**A**) The DNA pool described in **Fig. 1** are sandwiched in between Illumina sequencing adapters and synthesized on the flow cell surface. (**B**) NGS library was sequenced on a *MiSeq* chip through standard PE75 protocol and was denatured to expose ssDNA on the chip surface. Control sequences (i.e., PhiX) were labeled with an Atto488-tagged probe (fiducial marker). (**C**) To image SARS-CoV-2 spike protein binding on the chip, we first incubated the flow cell with 100 nM His-tagged spike protein trimer, which was then stained by the Alexa647 His-tag antibody conjugate. After imaging, the chip was regenerated by 0.1 N NaOH treatment, with another spike protein variant added in the following round. (**D**) A representative field of view (FOV) of PhiX labeled with Atto488-tagged probes (left, top) for mapping purpose, and WT spike protein labeled with Alexa647-His-tag antibody conjugate (right, top). The polonies representing the PhiX sequences, the seeding aptamer Apt2 and the negative control sequence (Scr) are highlighted in green (left, middle), yellow and light gray (right, middle) circles, respectively, which were identified after the CHAMP alignment. The merged figures (bottom) show the successful mapping of sequence positions and the chip images. Scale bars are 10 µm. (**E**) Corrected fluorescence intensities of the polonies correlating the seeding aptamers and the negative control sequence (Scr) on the chip when co-incubated with WT, Omicron$_{XBB}$, and Delta spike proteins, respectively. Error bars reflect the SEM (standard error of the mean) of each group. Number of duplicates of each trial can be found in **Supplementary Table S3**. *, $p < 0.05$; **, $p < 0.01$; ***, $p < 0.001$; ns, $p > 0.05$.

Enhancing the Affinity for Delta by Modifying the Aptamer Stem

Here we sought to identify mutants with improved binding to the Delta strain, as a proxy for adaptation to an earlier stage of SARS-CoV-2 evolution. We quantified the percentage change in fluorescence signal for each sequence relative to original Apt2 (hereafter referred to as percentage change) across three independent screening trials, each performed against a different strain. Analysis of the combined WT and Delta screening data showed that most sequences showed significantly lower binding to WT compared to Apt2, while approximately half pool exhibited enhanced binding to Delta (**fig. S5**). Nevertheless, because the fluorescence signals of Apt2 and Scr were less clearly separated for Delta (**Fig. 2E**), the corresponding calculated percentage changes could be less reliable. This limitation was further revealed by streptavidin-mediated surface binding assays (**fig. S1B**), where several high-fluorescence candidates failed to show consistently enhanced binding in ELONA (e.g., T3C-A39C; **Fig. 3C** and **fig. S6**).

To overcome the challenge, we changed the strategy by examining binding patterns at the sequence level using the screening data. The effects of individual sequences on a given viral strain were summarized as percentage changes and visualized across a series of heatmaps. Single mutants (**Fig. 3A**) and indels (**fig. S7**) binding data against Delta revealed that the 20-nt loop motif (residues C12 to T31) was also conserved for Delta binding, since any point mutation or insertion within this region disrupted interaction. Double-mutation heatmap on the stem further showed that the bases close to the loop are also intolerant with mutations (**fig. S8**). Based on this observation, we restricted subsequent analysis to mutants with alterations confined to the stem region to preserve Delta binding. These candidates were ranked according to the difference in percentage change between WT and Delta, with the goal of minimizing cross-reactivity. Top five sequences were selected for further evaluation (**Fig. 3B**). The binding profiles were validated outside the chip using ELONA (**Fig. 3C**). Most candidates exhibited binding profiles similar to that of the original Apt2. Among them, A8G-A39T showed a modest improvement in binding affinity for Delta relative to Apt2 (k_d ~20±4 nM vs. 89±10 nM). Notably, this variant retained very strong binding to WT (k_d ~0.8±0.2 nM) and negligible affinity for $\text{Omicron}_{\text{XBB}}$ (**Fig. 3D**).

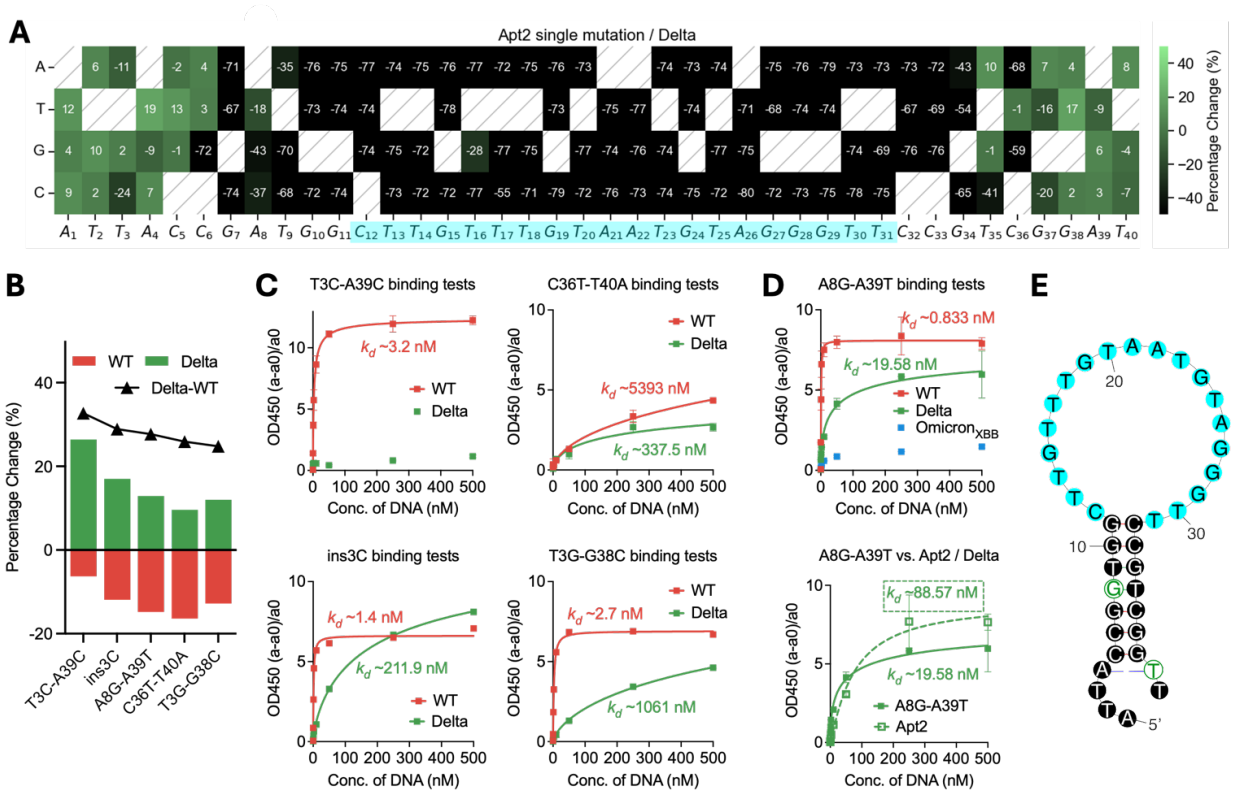

Fig. 3. Identifying Apt2-A8G-A39T as an improved Delta binder. (**A**) Apt2 single-mutation/Delta heatmap. The color of each cell represents the percentage change compared to the original Apt2/Delta with the color bar showing on the right. Cells representing the unmutated sequences are shown as diagonally hatched. The heatmap implied the immutability of the loop motif (highlighted in cyan). (**B**) Top five stem-altered candidates ranked by the Delta-WT percentage-change difference. Percentage changes for WT and Delta are shown as red and green bars, respectively. The black line indicates the Delta-WT percentage-change difference. (**C**)-(**D**) ELONA revealed that among all 5 candidates, A8G-A39T can bind slightly stronger than the seeding aptamer Apt2 (k_d ~20±4 nM vs. k_d ~89±10 nM, right). Further investigation showed that A8G-A39T has a similar binding pattern to the original Apt2, which is a strong WT binder (k_d ~0.8±0.2 nM), medium Delta binder, and does not bind Omicron$_{XBB}$. (**E**) A8G and A39T substitutions (highlighted by the green circles) were highlighted in the mFold-predicted secondary structure of Apt2. The motif was highlighted in cyan.

Identification of Omicron$_{XBB}$ Binders

To assess whether our platform can identify strands targeting more recent variants, we screened the designed pool for Omicron$_{XBB}$ binders. Most fluorescence signals were comparable to those of Apt2 and Scr (**Fig. 4A**), indicating that the majority exhibit weak or no binding to Omicron$_{XBB}$. Notably, a small subset displayed a pronounced increase in fluorescence intensity and was selected for further investigation. To improve binding specificity and reduce background from multi-target screens, we narrowed the selection to five candidates with negligible signals in both the WT and Delta screens (**Fig. 4B**, highlighted in blue). Among these, two were double mutants with the mutated bases positioning within the 20-nt loop motif, while three originated from the doped mutation subgroup (**Fig. 4B**, zoom-in), suggesting that unlike WT and Delta, the loop motif is insufficient to support Omicron$_{XBB}$ binding (**figs. S11-12**).

A streptavidin-mediated surface binding assay was used to evaluate the binding profiles of

the five selected sequences (**Fig. 4C**). In this assay, aptamer candidates were immobilized on streptavidin-coated microwell plates via a biotin moiety. His-tagged spike proteins and an anti-His-fluorophore conjugate were sequentially introduced, with washing steps between incubations (**Methods**; **fig. S1B**). Fluorescence intensities were measured using a plate reader and converted to percentage changes relative to the Apt2/WT positive baseline. Four of the five candidates suppressed binding to WT and Delta but fail to exhibit improved binding to $\text{Omicron}_{\text{XBB}}$. In contrast, doped854, a triple mutant (T17G-T23G-T25G; **Fig. 4D**), was able to exhibit binding to $\text{Omicron}_{\text{XBB}}$. This result was further supported by ELONA (**Fig. 4E**), which confirmed that doped854 binds $\text{Omicron}_{\text{XBB}}$ with much higher affinity than the original Apt2 (k_d ~7±0.9 nM vs. undetectable).

To investigate structural features underlying doped854's unique binding behavior, we examined its ability to activate thioflavin T (ThT), a fluorogenic dye sensitive to G-quadruplex (G4) structures[66–70]. ThT fluorescence was measured in the presence of Apt2, doped854, a rationally designed G4-forming mutant (G4Apt2: C12G-T16G-T17G-T23G-T25G; **Fig. 4F**), and control sequences known to strongly activate (D-22AG-40 [67,70]) or not respond to ThT (cTBA [71,72]) at the same quantity. G4Apt2 was designed based on the canonical G-quadruplex motif ($G_{\geq 3}N_xG_{\geq 3}N_xG_{\geq 3}N_xG_{\geq 3}$)[73]. All three aptamer mutants enhanced ThT fluorescence, with doped854 producing a 53% stronger signal than Apt2 in the screening buffer and G4Apt2 yielding an even larger increase (~90%). As expected, all signals were lower than that of D-22AG-40, a known G4 dimer (**Fig. 4G**). These results suggested that Apt2 does not form, or only weakly stabilizes, a G-quadruplex structure. Conversely, doped854 can form, or stabilize such a topology[74], which contributes to its ability to bind $\text{Omicron}_{\text{XBB}}$.

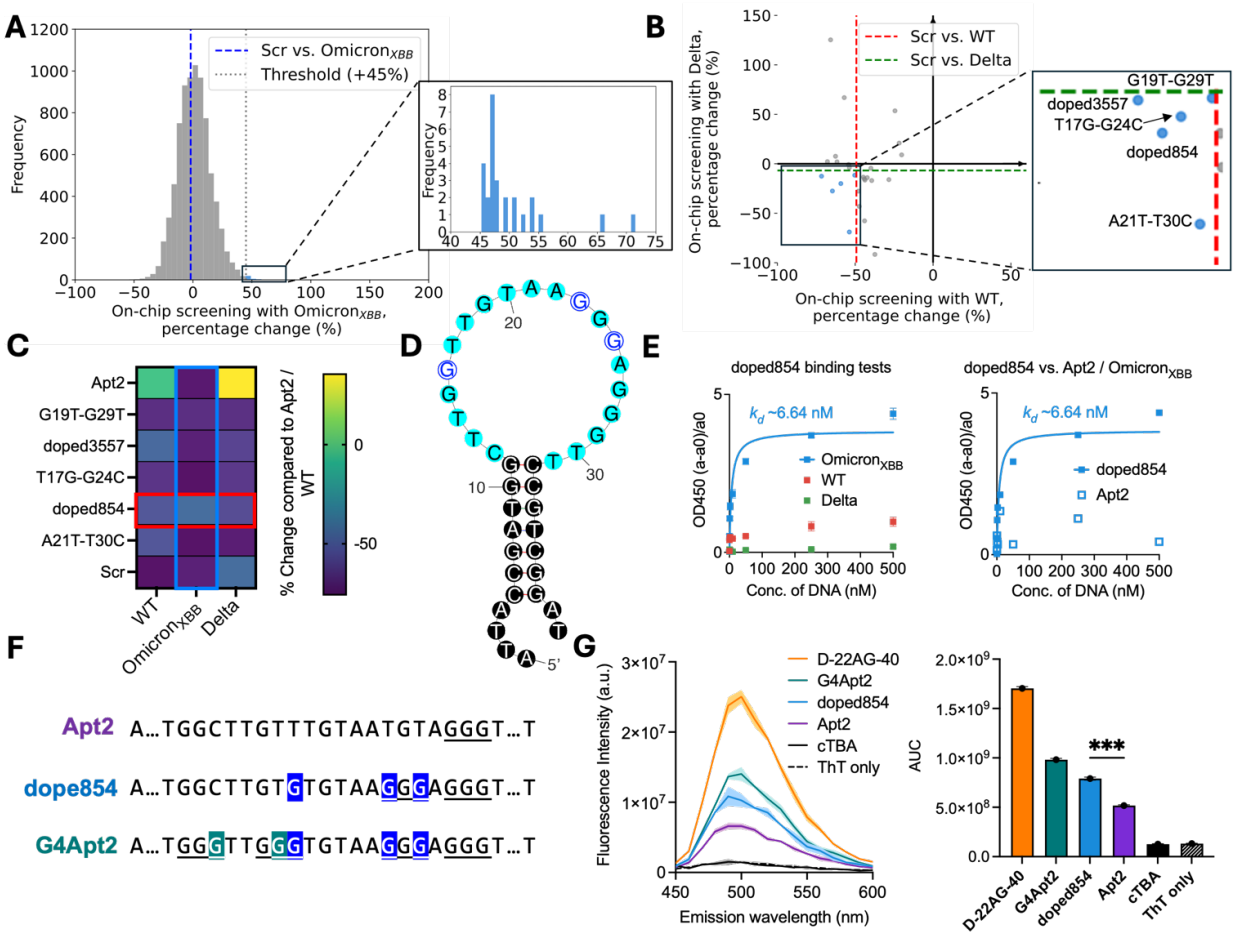

Fig. 4. Identifying Apt2-doped854 as an OmicronXBB-selective binder. (**A**) Sequences with at least +45% higher intensity than that of Apt2/Omicron$_{XBB}$ were selected out from the whole pool (bars in blue). (**B**) These selected candidates' WT and Delta binding data were retrieved and summarized in a scatterplot, with those with neglect binding affinity for WT (to the left of the red dotted line) and Delta (below the green dotted line) highlighted as blue puncta. (**C**) Streptavidin-mediated surface binding assay was used to test the bindings of Omicron$_{XBB}$ candidates selected from (**A**)-(**B**). Promising candidate doped854 was highlighted in a red box. Binding affinity for Omicron$_{XBB}$ comparison among the candidates are highlighted in a blue box. The color scale is shown on the right. (**D**) T17G, T23G and T25G substitutions (highlighted by the blue circles) were indicated in the mFold-predicted secondary structure of Apt2. The loop motif was highlighted in cyan. (**E**) ELONA revealed that Apt2-doped854 can bind Omicron$_{XBB}$, developing a new binding feature compared to the original Apt2 (k_d ~7±0.9 nM vs. undetectable). (**F**) Sequences of Apt2, doped854 and G4Apt2. Residues T2 to A8, T31 to A39 were omitted. Mutated bases in doped854 were highlighted in blue and further altered bases in G4Apt2 were highlighted in teal. G-tracts (G3s) were underscored. (**G**) Fluorescence activation of thioflavin T by DNA strands. D-22AG-40 is a G4 dimer known for strongly enhancing ThT's fluorescence. cTBA is the reverse complementary sequence of thrombin's aptamer TBA, which has no guanine in the sequence. Fluorescence was measured using 1 μM DNA and 1 μM thioflavin T. Shadings represent the standard deviations. Area under curve (AUC) was used to generate the overall intensities shown in the bar chart. Two-tailed un-paired *t* test was performed to compare the fluorescence intensities between doped854 and Apt2. P-value = 0.0001.

Enhancement of the Binding Specificity for the Wild-Type Strain by Mutation

Although Apt2 was originally selected against WT, it also binds the Delta strain (**Fig. 2B**). Beyond improving binding affinity, we attempted to optimize specificity toward WT, with the goal of identifying aptamers that preferentially recognize WT while minimizing cross-reactivity with Delta. By isolating WT-specific binders, we aimed to improve the precision of diagnostic tools. Highly specific detection of WT provides unambiguous strain assignment, which is essential for generating strain-resolved data to support studies of viral evolutionary pathways[75].

To identify potential sequence features associated with WT specificity, we compared the single-mutation heatmaps of Apt2 for WT (**fig. S9A**) and Delta (**Fig. 3A**), and found out that the G11 position, located at the junction between the loop and stem, tolerates a G to A substitution when binding WT, but this same mutation markedly disrupts binding to Delta (**Fig. 5A**). Consistent with this observation, the G11A single mutant showed minimal changes in binding $\text{Omicron}_{\text{XBB}}$ (**Fig. 5B**; +18%, +7%, and -75% for WT, $\text{Omicron}_{\text{XBB}}$, and Delta, respectively, compared to the original Apt2). WT double-mutation heatmap displayed a reddish horizontal stripe and a corresponding vertical stripe within the predominantly negative (dark) region (**fig. S10**), corresponding to the mutants where G11A is paired with a second mutated base either upstream or downstream of position 11. Notably, these cells with less negative values did not extend broadly across the heatmap, suggesting that retention of WT binding requires the second mutated base to be positioned away from the loop motif. Together, we hypothesized that Apt2 double mutants carrying G11A, combined with a second substitution outside the loop motif, might serve as selective WT binders. *MiSeq*-screening results for these double mutants are summarized in a series of bar plots (**Fig. 4C**). As expected, Delta binding was disrupted for all such double mutants, while WT binding varied depending on the type and position of the second mutated base.

For validation, we applied the streptavidin-mediated surface binding assay (**fig. S1B**) to a subset of G11A-containing double mutants. Mutants carrying substitutions at A1 or T40 were excluded, as they are more sensitive to be affected by interactions with chip adapters (**fig. S4**). All remaining candidates showed disrupted binding to Delta compared to Apt2. Among them, the point mutant G11A and the double mutants C5A-G11A, C5T-G11A, and G11A-C38G also exhibited noticeable reductions in WT signals (**Fig. 4D**). In contrast, the double mutants A4T-G11A and A4G-G11A displayed a WT-specific binding feature, with A4T-G11A (**Fig. 4E**) retaining the strongest binding to WT. We characterized the selected mutant A4T-G11A's binding kinetics toward the indicated strains (**Fig. 4F**). A4T-G11A retained strong binding affinity for WT, comparable to that of the parental Apt2 (k_d ~1±0.04 nM vs. 2±0.4 nM), while binding to Delta was markedly suppressed (k_d ~89±10 nM vs. undetectable). These results confirmed A4T-G11A as a strong and WT-specific binder for the SARS-CoV-2 spike protein trimer, demonstrating that sequence-level screening can simultaneously enable affinity optimization and effective counterselection.

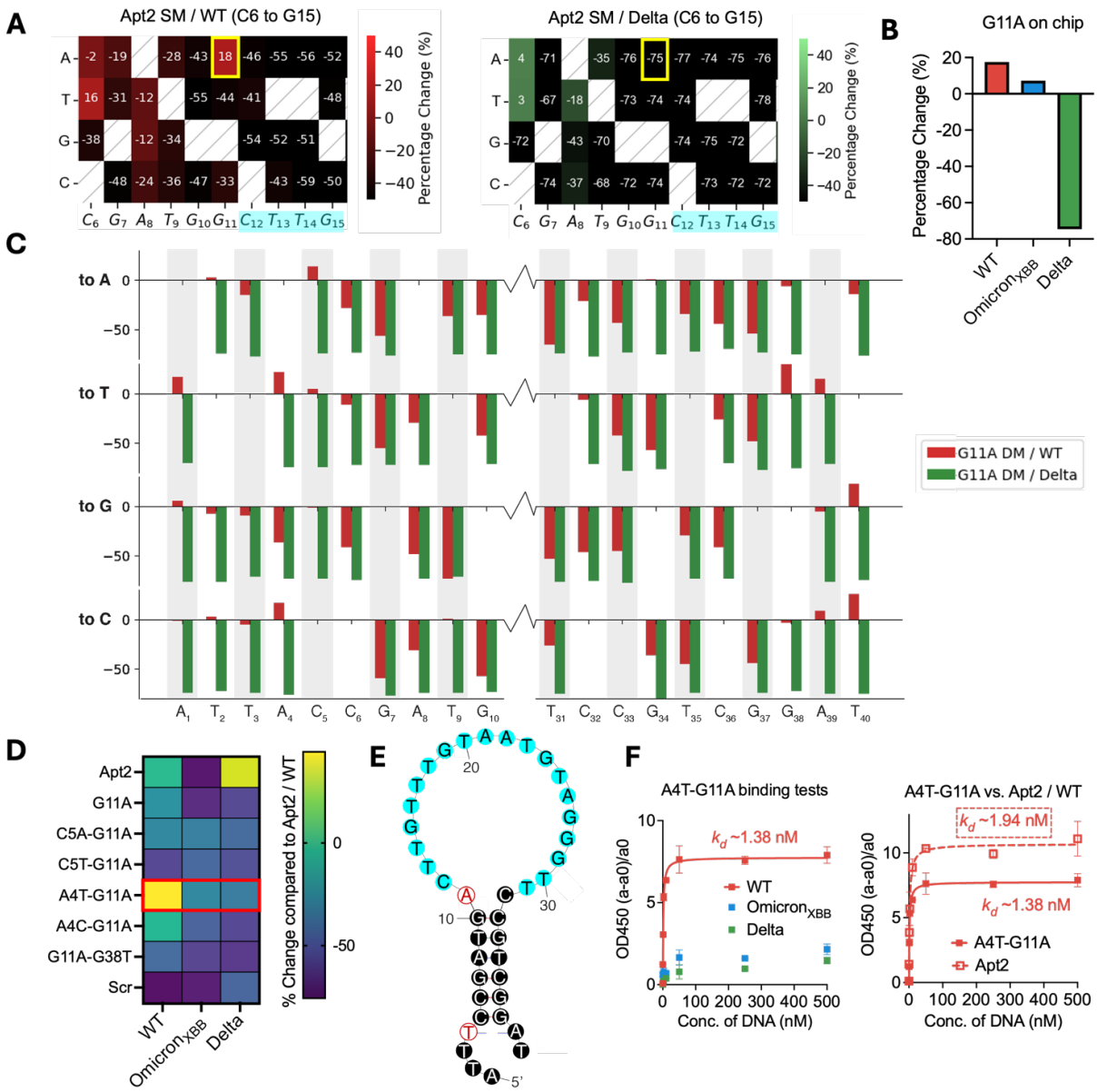

Fig. 5. Identifying Apt2-A4T-G11A as a more selective WT binder. (**A**) Part (residues C6 to G15) of the Apt2 single-mutation/WT (left, red) and Apt2 single-mutation/Delta (right, green) heatmaps. Bases within the loop motif were highlighted in cyan. G11A point mutation cells were highlighted in yellow boxes, which exhibited that G11A single mutants (SM) sustained the binding to WT but repressed the binding to Delta. Color bars are on the right of the heatmaps. Full heatmaps can be found in **fig. S6A** and **Fig. 3A**, respectively. (**B**) According to *MiSeq* screening, G11A's bindings to WT and Omicron$_{XBB}$ are similar to those of the original Apt2 (+18% and +7%), but G11A has a much lower binding to Delta (-75%). (**C**) Bar charts showed selected G11A-containing DMs' binding characteristics for WT (red) and Delta (green). The x axis represented the second mutation position; y axis showed the percentage change of the corresponding DM. (**D**) Streptavidin-mediated surface binding assay was used to test the bindings of WT-specific candidates selected from (**C**). The color scale is shown on the right. (**E**) A4T and G11A substitutions (highlighted by the red circles) were indicated in the mFold-predicted secondary structure of Apt2. The motif was highlighted in cyan. (**F**) ELONA showed that A4T-G11A remains to bind WT strongly (k_d

355 ~1±0.04 nM vs. k_d ~2±0.4 nM, right), while it efficiently suppresses the binding to Delta and showing no
356 detectable binding to $\text{Omicron}_{\text{XBB}}$ (left).

357

358 **Analyze the Binding Pattern of Apt2 with *MiSeq* Screening Data and Molecular Dynamics**
359 **Simulations**

360 Our platform can provide information beyond screening, by elucidating binding patterns
361 useful for rational design. Initially, it was assumed that the loop motif (residues C12 to T31) was
362 solely responsible for binding WT, with the stem serving only as a structural scaffold or a linker.
363 However, this assumption was challenged by several observations. First, the previously identified
364 Delta-enhanced binder A8G-A39T, which also showed improved WT binding, converted the
365 A8·T35 Watson-Crick base pair into a G8·T35 wobble pair, a change expected to destabilize the
366 structure. Second, the single mutant T9C, which should stabilize the stem by converting a T9·G34
367 wobble pair into a C9·G34 WC pair, instead completely abolished binding to all SARS-CoV-2
368 spike protein variants, both on chip (**fig. S9A**) and in ELONA (**Fig. 6A**). Further analysis revealed
369 a functional asymmetry within the stem region. The upper three base pairs (T9·G34 to G11·C32)
370 were highly intolerant to substitution by alternative WC or wobble pairs, suggesting that their role
371 in binding extends beyond simple structural stabilization (**Fig. 6C**, above the dashed line). In con-
372 trast, the lower four base pairs (C5·G38 to A8·T35) exhibited substantially greater tolerance to
373 base-pair alterations (**Fig. 6C**, below the dashed line), indicating a more limited contribution to
374 protein binding.

375 To provide a molecular-level insight into the possible aptamer binding pattern, we further
376 applied molecular dynamics (MD) simulations to investigate the structural behavior of the aptamer
377 strands (**fig. S13-14**)[76]. Structural superpositions of two most populated cluster representatives
378 (**Fig. 6B**), RMSF (Root-Mean-Square Fluctuation)[77] results (**Fig. 6D**) and the simulation trajecto-
379 ries (step = 100, **Supplementary Movies 1-3**) showed that Apt2, G11A and doped854 had very
380 flexible tail parts (residues A1 to A4, A39 to T40, green), and equally rigid stem (C5·G38 to
381 G11·C32, magenta) through the simulations, suggesting that (i) truncating the 4-nt tail might not
382 affect the binding[78]; (ii) The upper stem (T9·G34 to G11·C32) remains paired as predicted by
383 mFold, despite their additional role beyond structural stabilization; (iii) the alteration of the bind-
384 ing profiles could ascribe to the different sub-structures formed within the loop. Within the loop,
385 residues T16 to T20 in the original Apt2 showed greater stability during the 10-ns simulation com-
386 pared to the Delta non-binders G11A and doped854. For the $\text{Omicron}_{\text{XBB}}$, residues A21 to T25
387 displayed distinct stabilization, coinciding with two of the three mutations that form a consecutive
388 G tract and lead to an alternative folded conformation, which aligns with the observations from
389 the ThT experiments (**Fig. 4G**). The loop regions exhibited sharp bending towards the stems, sug-
390 gesting that the role of the upper stem might be to turn the aptamer into a preferred orientation to
391 facilitate the binding, rather than to directly contact the proteins.

392 In addition, according to the RMSF plot, the G11A single mutant did not pose too much
393 effect on the behavior of itself or neighboring bases; instead, it probably altered the binding selec-
394 tivity by inducing the structure change in the loop. To investigate the G11A single mutant's binding
395 mechanism, we performed two more simulations on G11C and G11T for comparison (**figs. S15-**
396 **16**). On one hand, G11A and G11T share relatively similar conformations; however, with the latter
397 one's structure much more dynamic and unstable according to the RMSF analysis (**Fig. 6F**). On
398 the other hand, G11C held a distinct 3D structure compared to G11A, G11T and the original Apt2:
399 G11C exhibits a uniquely inward-collapsed loop architecture centered along the short stem axis,

whereas Apt2, G11A and G11T adopt a more open and outward-projecting loop conformation, resulting in highly similar overall topologies which could enable the WT binding (**Fig. 6E**).

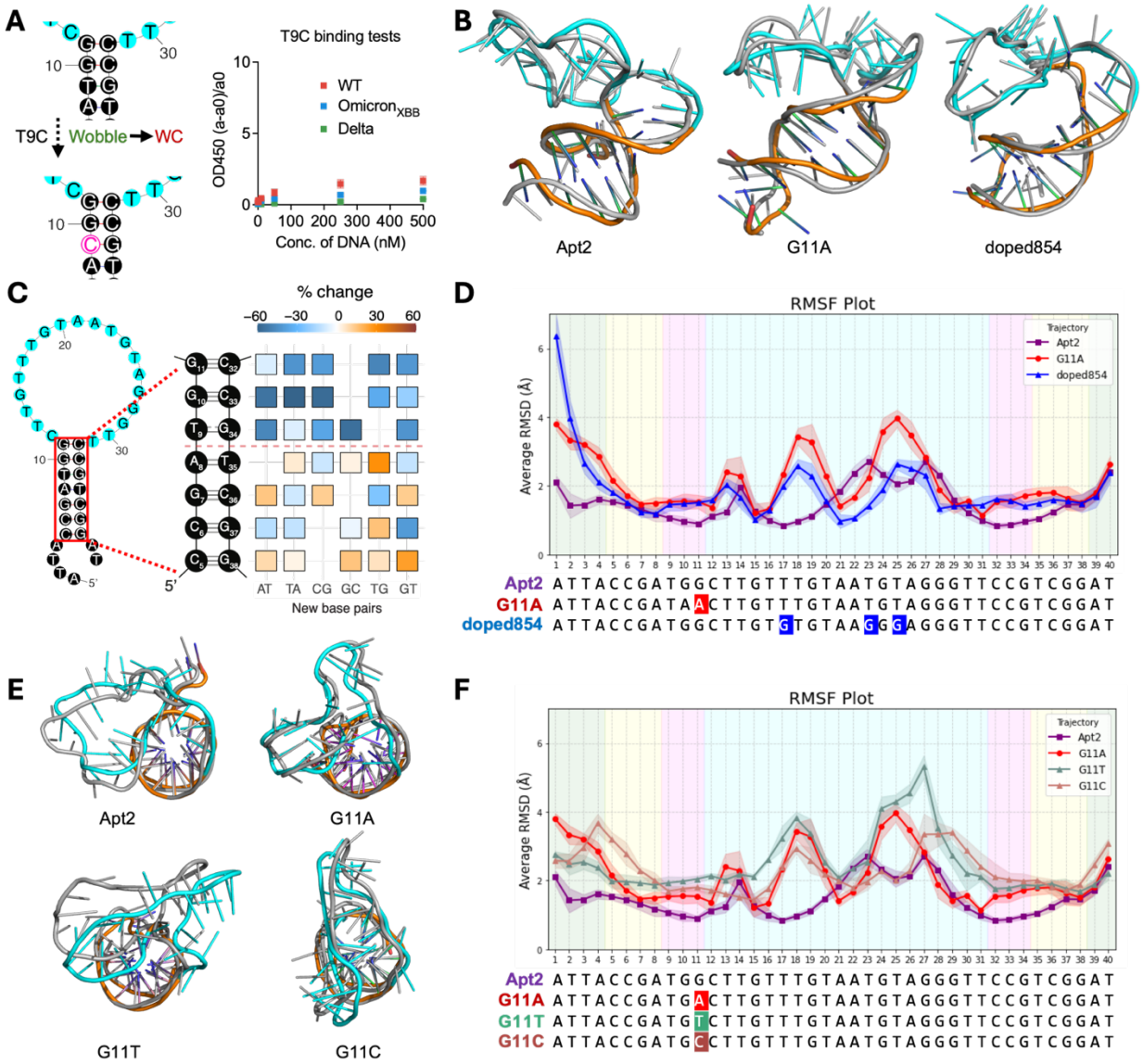

Fig. 6. Structure analysis with on-chip data and MD simulation. (**A**) ELONA for Apt2-T9C, indicating nearly no-binding to all spike protein variants. (**B**) Representative structures in each of the top two cluster superpositions within the latter 5 ns during the 10-ns simulation time of Apt2 (left; 33.6% and 33%), G11A (middle; 28.8% and 25%), and doped854 (right; 29.8% and 29.6%). The loop motifs were highlighted in cyan. The second top structures were highlighted in grey. (**C**) Base-pair-substitution heatmap for WT screening in the stem section. The x-axis indicates the new base pair for substitution; y-axis refers to the base pair being replaced. The pink dotted line separated base pairs with higher (below) and much lower (beyond) tolerance towards base-pair substitution. (**D**) RMSF (root-mean-square fluctuation) of Apt2, G11A and doped854. (**E**) Representative structures (top views) in each of the top two cluster superpositions within the latter 5 ns during the 10-ns simulation time of Apt2 (top left; 33.6% and 33%), G11A (top right; 28.8% and 25%), G11T (bottom left; 33.2% and 22.6%) and G11C (bottom right; 37% and 30.2%). The

loop motifs were highlighted in cyan. The second top structures were highlighted in grey. (**F**) RMSF of Apt2, G11A, G11T and G11C. Color code for (**D**) and (**F**): tails: green; lower stem: yellow; upper stem: magenta; loop (motif): cyan.

Selective Diagnostics for One of the Three Variant Strains with Strand Displacement Reaction

Here we demonstrate an application of the optimized aptamer through our platform, by converting the highly WT-selective aptamer A4T-G11A (**Fig. 5**) into a strand-displacement fluorescent sensor[79,80] specifically for SARS-CoV-2 WT spike protein detection. This design aimed to enhance diagnostic precision, as highly specific detection of WT enables unambiguous strain assignment, providing a foundation for generating strain-resolved data to inform studies of viral evolutionary pathways.

We have proven that the lower stem of the aptamer can be replaced by other base pairs (**Fig. 6C**), however, they cannot be truncated directly, based on the on-chip profiling results (**fig. S9C**). ELONA validation confirmed that truncation at C5·G38 yielded the shortest construct that retained strong WT binding (**fig. S19**). A4T-G11A was truncated, had the lower stem scrambled, and was extended on the 5' end[81–84] and labeled with FAM (denoted as wt sensor), allowing hybridization with an 11-nt Iowa Black quencher-labeled complementary strand (Q-cDNA, **Fig. 7A**). Quenching efficiency and baseline stability were evaluated prior to sensing measurements, with ~86% fluorescence quenching achieved at a 1:2 aptamer: Q-cDNA ratio (**fig. S20A**).

Upon addition of 200 nM WT spike protein, fluorescence was enhanced by ~3 fold, significantly exceeding the responses observed for Delta and $\text{Omicron}_{\text{XBB}}$ at the same concentration (**fig. S20B**). A calibration curve was constructed from the fluorescence enhancement upon WT addition with a four-parameter logistic (4PL) model (**Fig. 7B, left**)[85]. The response exhibited a linear relationship above 6.25 nM (**Fig. 7B, right**), from which a limit of detection (LOD) of 5.5 nM was estimated using 3σ/slope. In contrast, the responses to Delta and $\text{Omicron}_{\text{XBB}}$ remained near baseline, demonstrating strong specificity for the WT strain. We further evaluated sensor selectivity against a panel of common proteins (**Fig. 7C**). All non-target proteins produced negligible fluorescence changes, even at 5-fold higher concentrations (500 nM). Finally, the aptasensor maintained robust performance in complex biological matrices, retaining ~2-fold signal enhancement in 40% human serum (**Fig. 7D**), supporting its potential applicability in clinical samples[86–88].

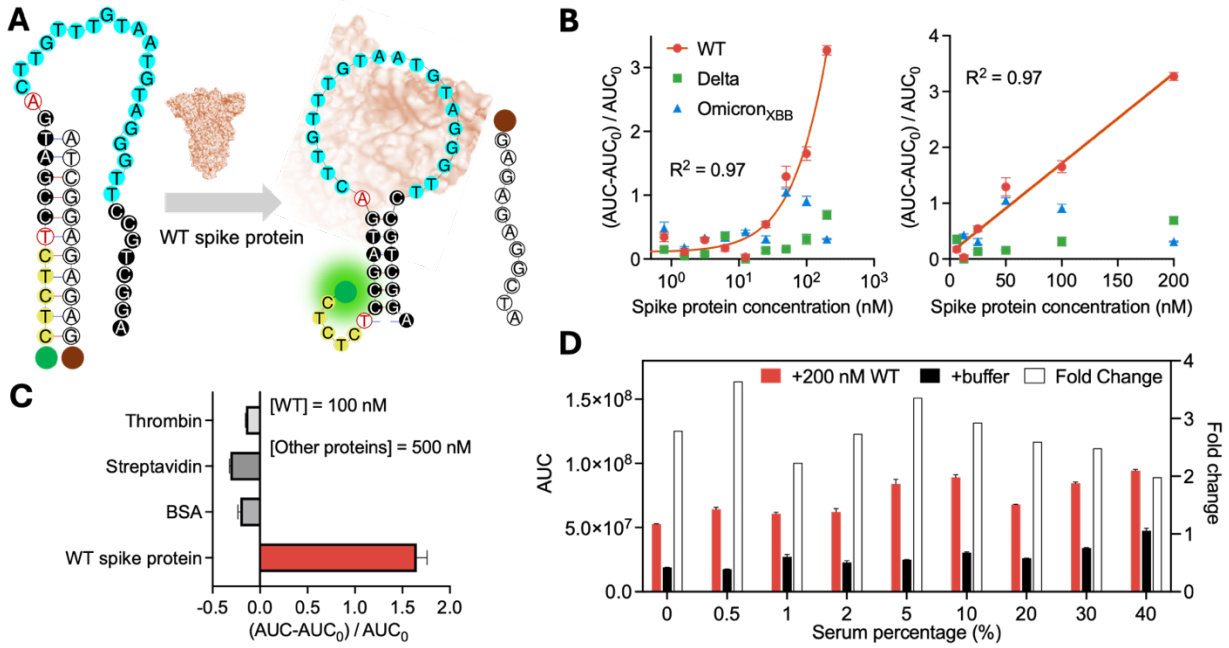

Figure 7. Precise diagnostics for SARS-CoV-2 WT with highly selective Apt2 mutant identified from the chip. (**A**) Schematic of the strand-displacement fluorescent sensor for rapid detection of SARS-CoV-2 spike proteins. The aptamer is modified with FAM (wt sensor), and the complementary DNA (cDNA) strand is modified with an Iowa Black quencher. Color code: loop: cyan; mutated bases: red circles; 5' overhang: yellow. (**B**) Calibration curves for WT spike protein detection. Data were fitted using a four-parameter logistic (4PL) model over the full concentration range (0.4-200 nM, left) and a linear model over the higher concentration range (6.25-200 nM, right). The limit of detection (LOD) was determined from the linear fit. (**C**) Selectivity analysis of the aptasensor against a panel of proteins. Non-target proteins were tested at 5× higher concentrations than the WT spike protein. (**D**) Stability and reactivity of the WT selective aptasensor in response to 200 nM WT spike protein across varying serum percentages (0-40%). For (**B**)-(**D**), each condition was measured in duplicate.

DISCUSSION

Here we demonstrate a massively parallel strategy for rapidly diversifying and screening spike-protein-binding aptamers within days, enabling either retention of binding to newly emerged viral strains or enhancement of specificity toward a particular strain. Starting from an early WT-spike protein aptamer Apt2, we were able to identify a mutant with improved binding to the Delta strain, a nM-level binder for Omicron$_{XBB}$, and a WT-specific mutant with the binding selectivity significantly enhanced. The platform also provided systematic exploration of the sequence-function relationship, revealing the binding pattern structurally incorporated with molecular dynamics simulations. Finally, we turned the selected WT-specific aptamer into a strand-displacement fluorescence sensor, enabling the precise diagnostics for SARS-CoV-2 WT.

Although virus-targeting aptamers are unlikely to replace monoclonal antibodies (mAbs) in the foreseeable future because of intrinsic limitations, including rapid renal clearance, susceptibility to nuclease degradation, and limited ability to engage immune effector functions[89–91], nevertheless, aptamers remain attractive for biosensing and certain therapeutic applications because of their low production cost, high stability, small size, and low immunogenicity[92–94]. Our results highlight an additional advantage of aptamers: adaptability. Once an initial antiviral aptamer has

been identified, it can be rapidly reengineered to recognize newly emerging variants without requiring de novo selection each time. In addition to improving binding to evolved strains, this study also demonstrates that aptamers can be tuned for strain-selective recognition, which may be particularly valuable for diagnostic applications requiring precise variant discrimination and for generating strain-resolved datasets to support studies of viral evolution[75,95–97]. We also demonstrated that aptamers offer functionality beyond binding[98] by converting a WT-selective variant into a strand-displacement fluorescent sensor. Their ability to be readily engineered into structure-switching aptasensors[79,88] provides a functional advantage over mAbs in certain sensing and diagnostic applications.

Repurposed NGS platforms offer a unique advantage for aptamer engineering by enabling massively parallel and quantitative interrogation of large, closely related sequence spaces in a single experiment. Prior studies[36,40,43–45,47,48,53,59], including our own[55,57,58,99], have demonstrated the versatility of this approach across diverse molecular systems, establishing repurposed NGS flow cells as a broadly useful platform for functional screening and sequence-property mapping. In this context, the key strength of NGS-based screening is not only throughput, but also the ability to retain and evaluate sequence diversity directly, rather than relying on iterative enrichment steps. This work extends this capability to a distinct challenge of rapid adaptation of antiviral aptamers to continuous viral evolution. Rather than treating each novel viral variant as a de novo discovery problem, we show that a repurposed NGS platform can be used to reengineer an existing functional aptamer through a random-rational hybrid diversification around a validated seeding aptamer. This strategy preserves the efficiency of high-throughput screening while introducing a more directed and adaptable framework for molecular redesign. As a result, the platform supports both rapid recovery of binding toward newly emerged variants and deliberate tuning of strain specificity, highlighting a specific advantage of our approach over existing repurposed NGS applications: it is not limited to characterizing or optimizing static molecular functions, but can instead be used to keep pace with an evolving biological target. The ability to iteratively screen related sequence libraries on the same platform further strengthens its practical value for emerging-pathogen surveillance and response.

Beyond the *MiSeq* screening, molecular dynamics simulations provide a structural framework for interpreting the variant-dependent binding behaviors observed experimentally (**Fig. 6**). These results suggest that the upper stem region, rather than serving solely as a passive scaffold, contributes directly to target recognition. Within the loop, distinct segments appear to govern variant-specific interactions, indicating that binding specificity is distributed across multiple localized motifs rather than confined to a single region. Notably, substitutions at position G11 exert a pronounced effect on global conformation. While the adenine substitution preserves a loop orientation compatible with binding, alternative substitutions lead to structural rearrangements or destabilization that disrupt target interaction. This provides a structural explanation for the experimentally observed selectivity at this position. Importantly, this suggests that aptamer optimization need not rely solely on empirical screening, but can be guided by structural considerations, providing a foundation for rational aptamer design in response to evolving viral targets.

More broadly, this work addresses a challenge highlighted by the COVID-19 pandemic: the lack of a modular molecular-recognition platform that can be readily reprogrammed to keep pace with viral evolution. Although the demonstration here was SARS-CoV-2 spike protein, this strategy should be extendable to other viral targets. In a future outbreak scenario, this could enable a practical workflow in which libraries diversified around an existing antiviral aptamer are prepared on repurposed NGS flow cells and screened immediately against newly emerging variants.

The library size can also be scaled up by utilizing other types of NGS flow cells (*MiSeq*, *HiSeq* and *NextSeq* and *NovaSeq*) or leveraging multiple chips. Because these chips can remain functional for years under appropriate storage (when soaked in an appropriate buffer and stored at 4 °C) and can be reused for sequential assays, the same platform could support iterative screening as new strains arise, without requiring complete library redesign unless full target escape occurs.

In summary, we developed a new method to rapidly evolve aptamers against newly emerging viral strains, providing a potential tool for responding to current and future pandemics. We demonstrated its effectiveness by identifying sequences that bind the 9-amino-acid-mutated Delta variant and the 39-amino-acid-mutated $\text{Omicron}_{\text{XBB}}$ variant within a diversified pool based on Apt2, which was originally selected against the baseline strain WT. This streamlined workflow can be readily adapted to a broad range of biomedical applications in the future.

MATERIAL AND METHODS

Doped pool mutation probability calculation

Let the number of the doped bases be L and the mutation rate be m. The theoretical number of the mutated bases n follows the binomial distribution.

$$n \sim binomial(L, m)$$

$$Pr_0(n|m, L) = \binom{L}{n} m^n (1-m)^{L-n}$$

With the n>2 filtration, the ultimate probability of n given m and L can be calculated as follows.

$$Pr(n|m, L) = \begin{cases} 0, & n < 3 \\ \dfrac{Pr_0(n|m, L)}{1 - \sum_0^2 Pr_0(i|m,\ L)}, & n \geq 3 \end{cases}$$

In this study, we set L = 20 (only dope the loop region) and m = 0.1. The theoretical and actual frequency of each mutation number can be found in **fig. S2**.

Apt2 library construction for NGS sequencing

Apt2 variants library with PCR primers was synthesized by Twist Biosciences. Forward and reverse PCR primers with Illumina sequencing adapters were synthesized by IDT. The overlap extension PCR process was performed using Q5 High-Fidelity 2× Master Mix from NEB (#M0492) following protocol provided by the manufacturer using a thermal cycler (Applied Biosystems). After PCR amplification, the library amplicons were purified with the PCR cleanup kit (#T1030, Monarch). The length of the amplicons was checked with a 2% agarose gel (**fig. S21**). The concentration and quality of the purified library amplicons was quantified using a NanoDrop 2000 UV-Vis spectrophotometer (Thermo Scientific). After PCR process, PhiX control V3 sequences (#FC-110-3001, Illumina) were diluted and mixed with Apt2 amplicons to prepare a 20 µl of 2 nM solution according to the requirement of our sequencing facility. The coverage for both PhiX and the library sequences were targeted to be 15% ~ 20% of overall sequencing space. The mixture was then subjected to *MiSeq* PE75 sequencing and the final loading concentration was at 8 pM.

567 **Illumina *MiSeq* chip preparation**
568 After sequencing, *MiSeq* chips were stored at 4°C in 20 mM sodium phosphate buffer (SPB, pH
569 6.6). Before experiments, the *MiSeq* chip was incubated with 20 µl 0.1 N NaOH solution for 5 min
570 at room temperature and rinsed with 20 µl 20 mM SPB (pH 6.8) 3 times to remove excess NaOH.
571 This step was to denature DNA strands which might contain residual fluorescent dyes from the
572 sequencing process. The chip was further photobleached by sequentially exposing each FOV (5
573 rows, 65 FOVs per row, 2 layers, 220 × 220 μm^2 each FOV) under an 80% excitation power for 1
574 min. The PhiX sequences were then labeled using an Atto488-tagged probe (1 µM and 20 µl) at
575 37°C for 40 min. The flow cell was rinsed 3 times by the screening buffer (40 mM Tris-HCl (pH
576 7.5), 150 mM NaCl, 6 mM $MgCl_2$, 2.5 mM $CaCl_2$, 2.5 mM KCl, 0.1% Tween 20, 0.2 mg/mL BSA)
577 to remove excess fluorophores. 20 µL 100 nM of His-tagged SARS-CoV-2 spike protein variants
578 (#SPN-C52H3, #SPN-C52He, #SPN-C5248; Acro Biosystems) were then introduced to the chip
579 surface by pipetting and incubated at 37°C for 1 hour. The protein was stored in nuclease-free
580 water at 1 µM and further diluted in screening buffer at room temperature for 30 min. The flow
581 cell was rinsed 3 times by the screening buffer to remove unbound proteins. 20 µL of 6×-His-tag
582 mAb-Alexa647 conjugate (#MA1-21315-A647, Invitrogen) were then introduced to the chip sur-
583 face by pipetting and incubated at room temperature for 15 min. The mAb-dye conjugate was
584 diluted at 1:500 ratio with the screening buffer. Excess conjugate was washed away with screening
585 buffer.
586
587 **Fluorescence microscopy and chip image acquisition**
588 An open-source software, Micro-Manager[100], was used to control an sCMOS camera (ORCA-
589 Flash 4.0, Hamamatsu), an xyz translation stage (ProScan III, Prior Scientific), and an auto-shutter
590 (Lambda SC, Shutter Instrument) on an Olympus IX71 fluorescence microscope for all our *MiSeq*
591 screening experiments. An LED illuminator and a 60× water-immersion objective (UP-
592 LSAPO60XW, Olympus) were used in the IX71 system. The detailed setup of images acquisition
593 could be found in our previous reports[55,57]. In brief, for each round of experiments, we acquired 3
594 rows of TIFF images with 60 field of views (FOVs, 220×220 μm^2) per row on both sides of the
595 chip (totally 360 images). This covers 5.81 mm^2 surface area. For each row of images, we first
596 recorded fiducial marker images (1 second exposure time, green channel, Ex/Em: 480/40 nm,
597 535/50 nm), and then acquired spike protein images with red channels (Ex/Em: 620/60 nm, 700/75
598 nm, cat. no. 49006, Chroma) under the same imaging settings. The scanning step size (220 µm per
599 step) and exposure time at each position were all precisely controlled by our auto-scan algorithm
600 and shutter control.
601
602 **Illumina *MiSeq* chip regeneration**
603 After loading the samples to the chip and acquiring the images, the flow cell was regenerated by
604 digesting the proteins and denaturing the anchored DNA sequences. 20 µL proteinase K mix
605 (#P8107, NEB) was added to the flow cell by pipetting and incubated at 40°C for 2 hours. Excess
606 proteinase and protein fragments were washed away by 20 mM SPB buffer. This was followed by
607 a 0.1 N NaOH denaturation. Excess base was removed by 20 mM SPB buffer.
608
609 **Fluorescence image alignment algorithm**
610 To identify the sequences behind polonies, we applied a revised imaging alignment algorithm from
611 **C**hip-**H**ybridized **A**ssociated **M**apping **P**latform, or CHAMP [53], which was developed by Jung *et*
612 *al.* The detailed description of implementing CHAMP algorithm on epi-fluorescence-microscope-

acquired images could be found in our previous report[55,57]. In brief, FASTQ coordinates were first Gaussian blurred to build a synthetic image and then transformed into Fourier space. TIFF images were also Fourier transformed and performed cross-correlation with transformed FASTQ images to register the rough position of each TIFF image. If the maximum cross-correlation value is larger than that of control position (other positions with higher read density), this TIFF image will perform precision alignment using least-squares constellation mapping to the potential target region to find detailed parameters (e.g., scaling factor, rotation angle). The output files included the x-y coordinates and the corresponding sequence ID of each cluster within the FOV and were saved individually according to different image positions. To analyze our Apt2 images, we corrected the uneven illumination using flat-field correction and bootstrapped to compute the median intensity of each activator (baseline corrected) in order to rank the Apt2 mutants' brightness.

Flat-field correction

To correct the uneven illumination across each FOV. We implemented flat-field correction. A Gaussian-blur filter ($\sigma = 100$) was applied on each FOV itself to generate the flat-field reference image for each FOV. The corrected images used for the following analysis were computed as follows:

$$I_{corrected} = I_{aptamer}\text{-}I_{dark} \,/\, (I_{flat\text{-}field\ image}\text{-}I_{dark})$$

Where $I_{corrected}$ is the flat-field-corrected images, $I_{aptamer}$ is the original TIFF images acquired under red channel, $I_{flat\text{-}field\ image}$ is the TIFF image after Gaussian blurring, and I_{dark} is the dark image acquired using 1 second exposure time when illumination source is turned off. When calculating the percentage changes, the intensities were subtracted by 1 to remove the average background from the protein and dye's non-specific binding to the chip surface.

ELONA binding assay

The binding affinities quantified in this study were all produced with ELONA [63] (enzyme-linked oligonucleotide assay). Briefly, 96-well high-binding microplates (#3690, Corning) were coated with the SARS-CoV-2 spike protein variant at a concentration of 1.33 µg/mL in PBS (pH 7.4, Invitrogen #AM9624) and incubated at 4 °C overnight. After washing with PBST (PBS containing 0.05% Tween-20), wells were blocked with blocking buffer (5% w/v BSA in PBST) for 1 hour at room temperature. Biotin-labeled aptamers (IDT) at various concentrations (3 duplicates for each concentration) were then added and incubated for 90 min at room temperature to allow binding. After washing, bound aptamers were detected using streptavidin-HRP conjugate (#RABHRP3-600UL, Millipore Sigma), followed by addition of TMB substrate (#555214, BD Bioscience). Washing was introduced between the steps with the screening buffer. The reaction was stopped with stop solution (10% H_2SO_4), and absorbance was measured at 450 nm using a microplate reader (SpectraMax i3, Molecular Devices). Control with scrambled Apt2 (Scr) were included. OD450 values were normalized with the lowest value on the whole plate.

$$OD450_{normalized} = (OD450_{raw} - OD450_{min})/OD450_{min}$$

The dissociation constant (k_d) was generated by fitting the concentration (c)-absorbance (A) curve to a Hill equation with a dynamic Hill slope (h), given that the signal produced by an enzymatic reaction might not be in a strictly linear relation with the binding. Each of the 3 duplicates was

658 fitted to the model separately. The reported k_ds are composed of the mean k_d of the duplicates with
659 the standard deviation:
660

661 $$\frac{A - A_0}{A_0} = \frac{B_{max} c^h}{k_d + c^h}$$

662

663 **Streptavidin-mediated surface binding assay**
664 In addition to ELONA, streptavidin-mediated surface binding assay was also used to estimate and
665 compare the bindings for the DNA sequences and spike protein variants. Biotin-labeled aptamers
666 (IDT) at 2.5 µM (3 duplicates) were then added to the 96-well streptavidin-coated pre-blocked
667 black microplates (#15503, Thermo Fisher). and incubated for 2 hours at room temperature to be
668 anchored onto the plate surface. After washing, 33 nM spike protein variants were added and in-
669 cubated for 1 hour to allow binding, followed by addition of the 0.002× 6×-His-tag mAb-Alexa488
670 conjugate (#MA1-21315-A488, Invitrogen) for 30 min at room temperature. After washing away
671 excess conjugate, 100 µL screening buffer was added to each well to enable the fluorescence meas-
672 urement. Fluorescence was measured at Ex/Em 485/535 nm using the microplate reader. Control
673 with scrambled Apt2 (Scr) were included.
674

675 **3D structures prediction for Apt2 and its mutants of interests**
676 Starting from the predicted secondary structure of Apt2 by mfold[62], we replaced all Ts with Us to
677 generate its equivalent ssRNA rApt2. The corresponding 3D structures rApt2 was then modeled
678 and visualized in RNAComposer[101,102]. The preliminary 3D structure of Apt2 was then obtained
679 by substituting bases T back for U. To relax the aptamer system, a refinement process was carried
680 out based on molecular dynamics simulation to produce the input structure for the MD simulation.
681 The input structures of G11A, doped854, G11C, G11T was generated by performing mutagenesis
682 to the Apt2's 3D structure by PyMol[103].
683

684 **Molecular dynamics simulation of selected aptamers**
685 The 3D structures of Apt2 and mutants of interests were obtained as described in the previous
686 section. The structures were then soaked into a box of water with a size of 65Å × 65Å × 65Å.
687 Counter ions such as Na^+ were added to neutralize the system. Additional NaCl, KCl, $MgCl_2$ and
688 $CaCl_2$ were added to obtain salt concentrations of 150, 6, 2.5 and 2.5 mmol/L, respectively, to
689 mimic the correct buffer condition. The systems underwent restrained minimization and restrained
690 gradual heating processes to reach equilibration before 10-ns production simulation for analy-
691 sis[104,105]. All simulations in this study were performed with the AMOEBA polarizable force
692 field[106–108].

693 **Simulated frame clustering**
694 A pairwise RMSD (Root mean square deviation) matrix was computed from the aligned frames to
695 serve as the distance metric. We applied agglomerative hierarchical clustering to this matrix, iter-
696 atively merging the closest clusters based on a complete linkage method. The resulting dendrogram
697 was cut at a threshold of RMSD = 4 to partition the trajectory into distinct conformational states.
698 and then the centroid is taken as representative structure. The central frames were collected from
699 each cluster and superposed to visualize for each mutant of interests.

700 **RMSF calculations**

701 Root mean square fluctuation (RMSF) analysis was conducted to evaluate the flexibility of indi-
702 vidual residues within the backbones of aptamer structures during MD simulations . The RMSF
703 values were calculated over the equilibrated trajectory using PyLOOS, according to the equation:

704 $$(i) = \sqrt{\langle (r_i(t) - \langle r_i \rangle)^2 \rangle_t}$$

705 where $r_i(t)$ represents the position of atom i at time t, and $\langle r_i \rangle$ denotes its time-averaged position
706 after aligning each frame to the first one. Only the equilibrated portion of the trajectory (last 5
707 ns) was used for the calculation.

708 **Strand-displacement fluorescent sensor test**
709 The fluorescence aptasensor experiments were performed in a half-area black 96-well microplate
710 (#675076, Greiner Bio-One) using the microplate reader mentioned in the previous section. The
711 excitation wavelengths were set to 480 nm; the emission spectra were collected from 510-700 nm.
712 2.5 μL of 1 μM wt sensor, 40.5 μL of screening buffer and 2 μL of proteins at different concen-
713 trations were premixed in the wells and incubated at RT for 30 min. 5 μL of 1 μM Q-cDNA was
714 then added the wells before measuring the fluorescence. The fluorescence intensity for each sam-
715 ple was calculated through the area under curve (AUC) of the emission spectrum. For the spike-in
716 serum test, 50% human serum was used to yield buffer with 0-40% serum. The mixture was heat-
717 inactivated at 85°C for 10 min. The supernatant was collected as the new buffer. The data were
718 represented as $(AUC-AUC_0) / AUC_0$, where AUC_0 denotes the fluorescence with the mixture of 2
719 μL of screening buffer, and AUC was the fluorescence with 2 μL of protein addition.
720
721
722 **ACKNOLEDGEMENTS**
723 We thank L. Xu for helping generate **Fig. 5C** and **Fig. 6C**.
724
725 **Funding:** This work was supported by the National Science Foundation grants (CBET2432379
726 and CHE2404334 to H.-C. Yeh and CBET2235455 to H.-C. Yeh and Y. Lu) and the National
727 Institutes of Health grant (DA060543 to H.-C. Yeh and GM141931 to Y. Lu). P. Ren and Y. Wang
728 are grateful for the support by National Institutes of Health (R01GM106137), Welch Foundation
729 (F-2120), and the Cancer Prevention and Research Institute of Texas grant (RP210088). Y.-I.C.
730 was supported by Texas Global Faculty Research Seed Grants.
731
732 **Author Contributions:** Y. H., Z. Y., Y.-A. K., Y. Wu, Y. L. and H.-C. Y. discussed and defined
733 the project. H.-C. Y. and Y. L. supervised the project. Y. H. and Y.-A. K. designed the screening
734 library. Y. H. and K.K. L. and W.-R. C. performed chip screening experiments. Y. H. and Y.-A.
735 K. analyzed the champ results. Z. Y., Y. Wu and A.-T. N. helped design the binding characteriza-
736 tion assays. Y. H. and D. F.-A. performed the binding characterization assays. J. G., Y. Wang and
737 Y. H. performed and analyzed MD simulations. Z. Y. and Y. H. designed and performed the strand-
738 displacement fluorescent sensor tests. Y. H. and Y. C. developed Python and R scripts for data
739 illustration. Y. H. and K.K. L. performed gel electrophoresis experiments during the optimization
740 phase. Y.-I. C., S. H., T.D. N., S. K. and P. R. provided critical insights and contributed to the
741 discussion. S. S. optimized the buffer condition. Y. Wu, Y.-A. K., Z. Y., Y.-I. C and D. F.-A.
742 reviewed or revised the manuscript. Y. H. and H.-C. Y. wrote the article with editorial assistance
743 from all co-authors. H.-C. Y. supervised the project.

Competing interests: The authors declare no competing financial interest.

Data and materials availability: All data needed to evaluate the conclusions in the paper are present in the paper and/or the Supplementary Materials. Other data are available from the corresponding author upon reasonable request.

Supplementary Materials

Tables S1 to S3, Notes, Supplementary Figs. S1 to S21, Movies S1 to S3

755 **References**

1. COVID-19 cases | WHO COVID-19 dashboard. *datadot* https://data.who.int/dashboards/covid19/cases.
2. Dennehy, J. J., Gupta, R. K., Hanage, W. P., Johnson, M. C. & Peacock, T. P. Where is the next SARS-CoV-2 variant of concern? *The Lancet* **399**, 1938–1939 (2022).
3. Sanyaolu, A. *et al.* The emerging SARS-CoV-2 variants of concern. *Therapeutic Advances in Infection* **8**, 20499361211024372 (2021).
4. Abdool Karim, S. S. & de Oliveira, T. New SARS-CoV-2 Variants - Clinical, Public Health, and Vaccine Implications. *N Engl J Med* **384**, 1866–1868 (2021).
5. Sigal, A., Milo, R. & Jassat, W. Estimating disease severity of Omicron and Delta SARS-CoV-2 infections. *Nat Rev Immunol* **22**, 267–269 (2022).
6. Cevik, M. & Mishra, S. SARS-CoV-2 variants and considerations of inferring causality on disease severity. *The Lancet Infectious Diseases* **21**, 1472–1474 (2021).
7. SeyedAlinaghi, S. *et al.* Characterization of SARS-CoV-2 different variants and related morbidity and mortality: a systematic review. *Eur J Med Res* **26**, 51 (2021).
8. Hui, K. P. Y. *et al.* SARS-CoV-2 Omicron variant replication in human bronchus and lung ex vivo. *Nature* **603**, 715–720 (2022).
9. Zhang, M. *et al.* A systematic review of Vaccine Breakthrough Infections by SARS-CoV-2 Delta Variant. *Int J Biol Sci* **18**, 889–900 (2022).
10. Birhane, M. *et al.* COVID-19 Vaccine Breakthrough Infections Reported to CDC — United States, January 1–April 30, 2021. *MMWR Morb Mortal Wkly Rep* **70**, 792–793 (2021).
11. Gupta, R. K. & Topol, E. J. COVID-19 vaccine breakthrough infections. *Science* **374**, 1561–1562 (2021).
12. Hacisuleyman, E. *et al.* Vaccine Breakthrough Infections with SARS-CoV-2 Variants. *N Engl J Med* **384**, 2212–2218 (2021).
13. Menni, C. *et al.* Symptom prevalence, duration, and risk of hospital admission in individuals infected with SARS-CoV-2 during periods of omicron and delta variant dominance: a prospective observational study from the ZOE COVID Study. *The Lancet* **399**, 1618–1624 (2022).
14. Sheikh, A., McMenamin, J., Taylor, B. & Robertson, C. SARS-CoV-2 Delta VOC in Scotland: demographics, risk of hospital admission, and vaccine effectiveness. *The Lancet* **397**, 2461–2462 (2021).
15. Twohig, K. A. *et al.* Hospital admission and emergency care attendance risk for SARS-CoV-2 delta (B.1.617.2) compared with alpha (B.1.1.7) variants of concern: a cohort study. *Lancet Infect Dis* **22**, 35–42 (2022).
16. Jones, B. E. *et al.* The neutralizing antibody, LY-CoV555, protects against SARS-CoV-2 infection in nonhuman primates. *Sci Transl Med* **13**, eabf1906 (2021).
17. Hansen, J. *et al.* Studies in humanized mice and convalescent humans yield a SARS-CoV-2 antibody cocktail. *Science* **369**, 1010–1014 (2020).
18. Frei, L. *et al.* Deep mutational learning for the selection of therapeutic antibodies resistant to the evolution of Omicron variants of SARS-CoV-2. *Nat. Biomed. Eng* **9**, 552–565 (2025).
19. Hwang, Y.-C. *et al.* Monoclonal antibodies for COVID-19 therapy and SARS-CoV-2 detection. *J Biomed Sci* **29**, 1 (2022).
20. Cao, Y. *et al.* Omicron escapes the majority of existing SARS-CoV-2 neutralizing antibodies. *Nature* **602**, 657–663 (2022).

21. McCallum, M. *et al.* Molecular basis of immune evasion by the Delta and Kappa SARS-CoV-2 variants. *Science* **374**, 1621–1626 (2021).
22. Vandenberg, O., Martiny, D., Rochas, O., van Belkum, A. & Kozlakidis, Z. Considerations for diagnostic COVID-19 tests. *Nat Rev Microbiol* **19**, 171–183 (2021).
23. Ellington, A. D. & Szostak, J. W. In vitro selection of RNA molecules that bind specific ligands. *Nature* **346**, 818–822 (1990).
24. Demek, E. & Arroyo-Currás, N. General approach to achieving electrochemical aptamer-based sensor sensitivity of buffer in blood plasma. *npj Biosensing* **3**, 2 (2026).
25. Li, J. *et al.* Monitoring HIV Antiretroviral Therapy via Aptamer-Based Measurements in Preclinical Animal Models, in Human Plasma. *Advanced Sensor Research* **4**, 2400191 (2025).
26. Li, J. *et al.* Diverse high-affinity DNA aptamers for wild-type and B.1.1.7 SARS-CoV-2 spike proteins from a pre-structured DNA library. *Nucleic Acids Res* **49**, 7267–7279 (2021).
27. Liu, X. *et al.* Neutralizing Aptamers Block S/RBD-ACE2 Interactions and Prevent Host Cell Infection. *Angewandte Chemie International Edition* **60**, 10273–10278 (2021).
28. Song, Y. *et al.* Discovery of Aptamers Targeting the Receptor-Binding Domain of the SARS-CoV-2 Spike Glycoprotein. *Anal. Chem.* **92**, 9895–9900 (2020).
29. Amini, R. *et al.* Aptamers for SARS-CoV-2: Isolation, Characterization, and Diagnostic and Therapeutic Developments. *Analysis & Sensing* **2**, e202200012 (2022).
30. Kacherovsky, N. *et al.* Discovery and Characterization of Spike N-Terminal Domain-Binding Aptamers for Rapid SARS-CoV-2 Detection. *Angewandte Chemie* **133**, 21381–21385 (2021).
31. Silwal, A. P. *et al.* DNA aptamers inhibit SARS-CoV-2 spike-protein binding to hACE2 by an RBD-independent or dependent approach. *Theranostics* **12**, 5522–5536 (2022).
32. Shi, L. *et al.* Aptamer-Functionalized Nanochannels for One-Step Detection of SARS-CoV-2 in Samples from COVID-19 Patients. *Anal. Chem.* **93**, 16646–16654 (2021).
33. Silwal, A. P. *et al.* A universal DNA aptamer as an efficient inhibitor against spike-protein/hACE2 interactions. *Chem. Commun.* **58**, 8049–8052 (2022).
34. Li, J., Zhang, Z., Amini, R. & Li, Y. One Solution for All: Searching for Universal Aptamers for Constantly Mutating Spike Proteins of SARS-CoV-2. *ChemMedChem* **17**, e202200166 (2022).
35. Sun, M. *et al.* Spherical neutralizing aptamer suppresses SARS-CoV-2 Omicron escape. *Nano Today* **44**, 101499 (2022).
36. Tome, J. M. *et al.* Comprehensive analysis of RNA-protein interactions by high-throughput sequencing–RNA affinity profiling. *Nat Methods* **11**, 683–688 (2014).
37. She, R. *et al.* Comprehensive and quantitative mapping of RNA–protein interactions across a transcribed eukaryotic genome. *Proc. Natl. Acad. Sci. U.S.A.* **114**, 3619–3624 (2017).
38. Andreasson, J. O. L., Savinov, A., Block, S. M. & Greenleaf, W. J. Comprehensive sequence-to-function mapping of cofactor-dependent RNA catalysis in the glmS ribozyme. *Nat Commun* **11**, 1663 (2020).
39. Andreasson, J. O. L. *et al.* Crowdsourced RNA design discovers diverse, reversible, efficient, self-contained molecular switches. *Proc. Natl. Acad. Sci. U.S.A.* **119**, e2112979119 (2022).
40. Nutiu, R. *et al.* Direct measurement of DNA affinity landscapes on a high-throughput sequencing instrument. *Nat Biotechnol* **29**, 659–664 (2011).
41. Becker, W. R. *et al.* High-Throughput Analysis Reveals Rules for Target RNA Binding and Cleavage by AGO2. *Molecular Cell* **75**, 741-755.e11 (2019).
42. Layton, C. J., McMahon, P. L. & Greenleaf, W. J. Large-Scale, Quantitative Protein Assays on a High-Throughput DNA Sequencing Chip. *Molecular Cell* **73**, 1075-1082.e4 (2019).
43. Aguirre Rivera, J. *et al.* Massively parallel analysis of single-molecule dynamics on next-generation sequencing chips. *Science* **385**, 892–898 (2024).
44. Svensen, N., Peersen, O. B. & Jaffrey, S. R. Peptide Synthesis on a Next-Generation DNA Sequencing Platform. *ChemBioChem* **17**, 1628–1635 (2016).
45. Buenrostro, J. D. *et al.* Quantitative analysis of RNA-protein interactions on a massively parallel array reveals biophysical and evolutionary landscapes. *Nat Biotechnol* **32**, 562–568 (2014).

46. Ozer, A. *et al.* Quantitative assessment of RNA-protein interactions with high-throughput sequencing–RNA affinity profiling. *Nat Protoc* **10**, 1212–1233 (2015).
47. Porebski, B. T. *et al.* Rapid discovery of high-affinity antibodies via massively parallel sequencing, ribosome display and affinity screening. *Nat. Biomed. Eng* **8**, 214–232 (2023).
48. Severins, I. *et al.* Single-molecule structural and kinetic studies across sequence space. *Science* **385**, 898–904 (2024).
49. Fujita, H. *et al.* Discovery of high-specificity DNA aptamers for progesterone using a high-throughput array platform. 2025.09.13.675901 Preprint at https://doi.org/10.1101/2025.09.13.675901 (2025).
50. Gidi, Y., Hein, L. A., Fujita, H., Eisenstein, M. & Soh, H. T. Accelerated Discovery of Aptamer Beacons via Massively Parallel Screening. 2025.07.31.667975 Preprint at https://doi.org/10.1101/2025.07.31.667975 (2025).
51. Kuo, Y.-A. *et al.* Massively Parallel Selection of NanoCluster Beacons (Adv. Mater. 41/2022). *Advanced Materials* **34**, 2270286 (2022).
52. Kuo, H.-C., Prupes, J., Chou, C.-W. & Finkelstein, I. J. Massively parallel profiling of RNA-targeting CRISPR-Cas13d. *Nat Commun* **15**, 498 (2024).
53. Jung, C. *et al.* Massively Parallel Biophysical Analysis of CRISPR-Cas Complexes on Next Generation Sequencing Chips. *Cell* **170**, 35-47.e13 (2017).
54. Jones, S. K. *et al.* Massively parallel kinetic profiling of natural and engineered CRISPR nucleases. *Nat Biotechnol* **39**, 84–93 (2021).
55. Kuo, Y.-A. *et al.* Fluorogenic Aptamer Optimizations on a Massively Parallel Sequencing Platform. 2024.07.07.602435 Preprint at https://doi.org/10.1101/2024.07.07.602435 (2024).
56. Wu, D. *et al.* Flow-Cell-Based Technology for Massively Parallel Characterization of Base-Modified DNA Aptamers. *Anal. Chem.* **95**, 2645–2652 (2023).
57. Kuo, Y.-A. *et al.* Massively Parallel Selection of NanoCluster Beacons. *Advanced Materials* **34**, 2204957 (2022).
58. Nguyen, A.-T. *et al.* Massively Parallel Fluorescence Lifetime Screening of Mango Fluorogenic RNA Aptamer on an NGS Chip. (2025).
59. Yoshikawa, A. M., Wan, L., Zheng, L., Eisenstein, M. & Soh, H. T. A system for multiplexed selection of aptamers with exquisite specificity without counterselection. *Proc. Natl. Acad. Sci. U.S.A.* **119**, e2119945119 (2022).
60. Yoshikawa, A. M. *et al.* A massively parallel screening platform for converting aptamers into molecular switches. *Nat Commun* **14**, 2336 (2023).
61. Wan, L., Yoshikawa, A., Eisenstein, M. & Soh, H. T. High-Throughput Strategy for Enhancing Aptamer Performance across Different Environmental Conditions. *ACS Sens.* **8**, 2519–2524 (2023).
62. Zuker, M. Mfold web server for nucleic acid folding and hybridization prediction. *Nucleic Acids Res* **31**, 3406–3415 (2003).
63. Pawel, G., Ma, Y., Wu, Y., Lu, Y. & Peinetti, A. Binding Affinity Measurements Between DNA Aptamers and their Virus Targets Using ELONA and MST. *BIO-PROTOCOL* **12**, (2022).
64. Canoura, J. *et al.* Accelerating Post-SELEX Aptamer Engineering Using Exonuclease Digestion. *J. Am. Chem. Soc.* **143**, 805–816 (2021).
65. Wang, Q. *et al.* Fighting Mutations with Mutations: Evolutionarily Adapting a DNA Aptamer for High-Affinity Recognition of Mutated Spike Proteins of SARS-CoV-2. *Angewandte Chemie* **n/a**, e202415226 (2024).
66. VarnBuhler, B. S., Moon, J., Dey, S. K., Wu, J. & Jaffrey, S. R. Detection of SARS-CoV-2 RNA Using a DNA Aptamer Mimic of Green Fluorescent Protein. *ACS Chem. Biol.* **17**, 840–853 (2022).
67. Jing, S., Liu, Q., Jin, Y. & Li, B. Dimeric G-Quadruplex: An Effective Nucleic Acid Scaffold for Lighting Up Thioflavin T. *Anal. Chem.* **93**, 1333–1341 (2021).
68. Kataoka, Y. *et al.* Minimal Thioflavin T Modifications Improve Visual Discrimination of Guanine-Quadruplex Topologies and Alter Compound-Induced Topological Structures. *Anal. Chem.* **86**, 12078–12084 (2014).

69. Xu, S. *et al.* Thioflavin T as an efficient fluorescence sensor for selective recognition of RNA G-quadruplexes. *Sci Rep* **6**, 24793 (2016).
70. Mohanty, J. *et al.* Thioflavin T as an Efficient Inducer and Selective Fluorescent Sensor for the Human Telomeric G-Quadruplex DNA. *J. Am. Chem. Soc.* **135**, 367–376 (2013).
71. Bock, L. C., Griffin, L. C., Latham, J. A., Vermaas, E. H. & Toole, J. J. Selection of single-stranded DNA molecules that bind and inhibit human thrombin. *Nature* **355**, 564–566 (1992).
72. Schultze, P., Macaya, R. F. & Feigon, J. Three-dimensional Solution Structure of the Thrombin-binding DNA Aptamer d(GGTTGGTGTGGTTGG). *Journal of Molecular Biology* **235**, 1532–1547 (1994).
73. Maizels, N. & Gray, L. T. The G4 Genome. *PLOS Genetics* **9**, e1003468 (2013).
74. Jamroskovic, J., Livendahl, M., Eriksson, J., Chorell, E. & Sabouri, N. Identification of Compounds that Selectively Stabilize Specific G-Quadruplex Structures by Using a Thioflavin T-Displacement Assay as a Tool. *Chemistry – A European Journal* **22**, 18932–18943 (2016).
75. Han, A. X. *et al.* SARS-CoV-2 diagnostic testing rates determine the sensitivity of genomic surveillance programs. *Nat Genet* **55**, 26–33 (2023).
76. Bartley, S., Rhinehardt, K. & Dellinger, K. Investigating DNA Aptamer Binding to Domains of the SARS-CoV-2 Spike Protein: Insights from Molecular Dynamics and MM/PBSA Analysis. *ChemistrySelect* **10**, e202500900 (2025).
77. Martínez, L. Automatic Identification of Mobile and Rigid Substructures in Molecular Dynamics Simulations and Fractional Structural Fluctuation Analysis. *PLoS One* **10**, e0119264 (2015).
78. Díaz-Fernández, A. *et al.* Refinement and Truncation of DNA Aptamers Based on Molecular Dynamics Simulations: Computational Protocol and Experimental Validation. *J. Chem. Inf. Model.* https://doi.org/10.1021/acs.jcim.5c00243 (2025) doi:10.1021/acs.jcim.5c00243.
79. Nutiu, R. & Li, Y. Structure-Switching Signaling Aptamers. *J. Am. Chem. Soc.* **125**, 4771–4778 (2003).
80. Wilson, B. D., Hariri, A. A., Thompson, I. A. P., Eisenstein, M. & Soh, H. T. Independent control of the thermodynamic and kinetic properties of aptamer switches. *Nat Commun* **10**, 5079 (2019).
81. Wang, J., Liu, Y., Li, X., Lei, H. & Liu, J. A high affinity and selective DNA aptamer for copper ions. *Chem. Commun.* **60**, 14272–14275 (2024).
82. Xie, Y. *et al.* A Pair of DNA Aptamers That Can Selectively Bind to Bilirubin and Biliverdin. *ACS Chem. Biol.* **20**, 2028–2037 (2025).
83. Zhao, Y., Li, A. Z. & Liu, J. Capture-SELEX for Chloramphenicol Binding Aptamers for Labeled and Label-Free Fluorescence Sensing. *Environ. Health* **1**, 102–109 (2023).
84. Huang, P.-J. J. & Liu, J. Simultaneous Detection of L-Lactate and D-Glucose Using DNA Aptamers in Human Blood Serum. *Angewandte Chemie International Edition* **62**, e202212879 (2023).
85. Kim, S. *et al.* Mechanistic insights into the color transformation of a non-FRET substrate for RNase activity detection. 2026.03.11.710959 Preprint at https://doi.org/10.64898/2026.03.11.710959 (2026).
86. Xiao, Y., Piorek, B. D., Plaxco, K. W. & Heeger, A. J. A Reagentless Signal-On Architecture for Electronic, Aptamer-Based Sensors via Target-Induced Strand Displacement. *J. Am. Chem. Soc.* **127**, 17990–17991 (2005).
87. Son, K. *et al.* Continuous, Week-Long, Seconds-Resolved In Vivo Drug Measurements Performed with a Xenonucleic Acid-Employing Electrochemical, Aptamer-Based Sensor. *J. Am. Chem. Soc.* **148**, 10016–10025 (2026).
88. Baker, B. R. *et al.* An Electronic, Aptamer-Based Small-Molecule Sensor for the Rapid, Label-Free Detection of Cocaine in Adulterated Samples and Biological Fluids. *J. Am. Chem. Soc.* **128**, 3138–3139 (2006).
89. Wu, Y., Belmonte, I., Sykes, K. S., Xiao, Y. & White, R. J. Perspective on the Future Role of Aptamers in Analytical Chemistry. *Anal. Chem.* **91**, 15335–15344 (2019).
90. Keefe, A. D., Pai, S. & Ellington, A. Aptamers as therapeutics. *Nat Rev Drug Discov* **9**, 537–550 (2010).

91. Thomas, B. J., Porciani, D. & Burke, D. H. Cancer immunomodulation using bispecific aptamers. *Molecular Therapy Nucleic Acids* **27**, 894–915 (2022).
92. Nakatsuka, N. *et al.* Aptamer–field-effect transistors overcome Debye length limitations for small-molecule sensing. *Science* **362**, 319–324 (2018).
93. Yu, H., Alkhamis, O., Canoura, J., Liu, Y. & Xiao, Y. Advances and Challenges in Small-Molecule DNA Aptamer Isolation, Characterization, and Sensor Development. *Angewandte Chemie International Edition* **60**, 16800–16823 (2021).
94. Agnello, L., Camorani, S., Fedele, M. & Cerchia, L. Aptamers and antibodies: rivals or allies in cancer targeted therapy? *Explor Target Antitumor Ther* **2**, 107–121 (2021).
95. Wohl, S., Schaffner, S. F. & Sabeti, P. C. GENOMIC ANALYSIS OF VIRAL OUTBREAKS. *Annu Rev Virol* **3**, 173–195 (2016).
96. Wallace, Z. S. *et al.* Early detection of emerging SARS-CoV-2 variants of interest for experimental evaluation. *Front. Bioinform.* **2**, (2022).
97. Korber, B., Fischer, W. & Theiler, J. Real-time monitoring of SARS-CoV-2 evolution during the COVID-19 pandemic. *Cell Host & Microbe* **33**, 1802–1806 (2025).
98. Hariri, A. A. *et al.* Modular Aptamer Switches for the Continuous Optical Detection of Small-Molecule Analytes in Complex Media. *Advanced Materials* **36**, 2304410 (2024).
99. Chen, Y.-I. *et al.* Lifetime-based multiplexed detection of viral RNA using fluorogenic aptamers. 2026.04.13.718069 Preprint at https://doi.org/10.64898/2026.04.13.718069 (2026).
100. Edelstein, A. D. *et al.* Advanced methods of microscope control using μManager software. *J Biol Methods* **1**, e10 (2014).
101. Sarzynska, J., Popenda, M., Antczak, M. & Szachniuk, M. RNA tertiary structure prediction using RNAComposer in CASP15. *Proteins: Structure, Function, and Bioinformatics* **91**, 1790–1799 (2023).
102. Popenda, M. *et al.* Automated 3D structure composition for large RNAs. *Nucleic Acids Res* **40**, e112 (2012).
103. Schrödinger, L. & DeLano, W. PyMOL. (2020).
104. Romo, T. D. & Grossfield, A. LOOS: An extensible platform for the structural analysis of simulations. in *2009 Annual International Conference of the IEEE Engineering in Medicine and Biology Society* 2332–2335 (IEEE, Minneapolis, MN, 2009). doi:10.1109/IEMBS.2009.5335065.
105. Romo, T. D., Leioatts, N. & Grossfield, A. Lightweight object oriented structure analysis: Tools for building tools to analyze molecular dynamics simulations. *Journal of Computational Chemistry* **35**, 2305–2318 (2014).
106. Zhang, C. *et al.* AMOEBA Polarizable Atomic Multipole Force Field for Nucleic Acids. *J. Chem. Theory Comput.* **14**, 2084–2108 (2018).
107. Ponder, J. W. *et al.* Current Status of the AMOEBA Polarizable Force Field. *J. Phys. Chem. B* **114**, 2549–2564 (2010).
108. Jing, Z. *et al.* Polarizable Force Fields for Biomolecular Simulations: Recent Advances and Applications. *Annual Review of Biophysics* **48**, 371–394 (2019).

1